This is a repository copy of *Measurement of the spin temperature of optically cooled nuclei and GaAs hyperfine constants in GaAs/AlGaAs quantum dots*.

White Rose Research Online URL for this paper:
http://eprints.whiterose.ac.uk/116353/

Version: Supplemental Material

Article:

Chekhovich, E.A., Ulhaq, A., Zallo, E. et al. (3 more authors) (2017) Measurement of the spin temperature of optically cooled nuclei and GaAs hyperfine constants in GaAs/AlGaAs quantum dots. Nature Materials, 16 (10). pp. 982-986. ISSN 1476-1122

https://doi.org/10.1038/nmat4959

© 2017 Macmillan Publishers Limited, part of Springer Nature. This is an author produced version of a paper subsequently published in Nature Materials. Uploaded in accordance with the publisher's self-archiving policy.

Reuse

Unless indicated otherwise, fulltext items are protected by copyright with all rights reserved. The copyright exception in section 29 of the Copyright, Designs and Patents Act 1988 allows the making of a single copy solely for the purpose of non-commercial research or private study within the limits of fair dealing. The publisher or other rights-holder may allow further reproduction and re-use of this version - refer to the White Rose Research Online record for this item. Where records identify the publisher as the copyright holder, users can verify any specific terms of use on the publisher's website.

Takedown

If you consider content in White Rose Research Online to be in breach of UK law, please notify us by emailing eprints@whiterose.ac.uk including the URL of the record and the reason for the withdrawal request.

eprints@whiterose.ac.uk
https://eprints.whiterose.ac.uk/

Supplementary Information: Measurement of the spin temperature of optically cooled nuclei and GaAs hyperfine constants in GaAs/AlGaAs quantum dots

E. A. Chekhovich[1],* A. Ulhaq[1,5], E. Zallo[2,3], F. Ding[2,4], O. G. Schmidt[2], and M. S. Skolnick[1]

[1]*Department of Physics and Astronomy, University of Sheffield, Sheffield, S3 7RH, United Kingdom.*

[2]*Institute for Integrative Nanoscience, IFW Dresden,*
Helmholtz str. D-01069, Dresden, Germany.

[3]*Paul-Drude-Institut für Festkörperelektronik,*
Hausvogteiplatz 5-7, 10117 Berlin, Germany.

[4]*Institut für Festkörperphysik, Leibniz Universität Hannover,*
Appelstrasse 2, 30167 Hannover, Germany. and

[5]*School of Science and Engineering, Lahore University of Management Sciences (LUMS),*
Sector U, D.H.A, Lahore, 54792, Pakistan.

Supplementary Note 1. SAMPLE STRUCTURE.

The sample growth process has been reported in detail previously[1]. Here we give a brief description.

The nanohole filled droplet epitaxial quantum dot sample is grown via solid molecular beam epitaxy (MBE). The GaAs buffer layer is first grown and is followed by deposition of 11 monolayers of Ga at 520 °C forming Ga droplets. The droplets are then annealed under As flux resulting in crystallization and eventual formation of nanoholes due to As dissolution and Ga diffusion. The holes are then filled by depositing 7 nm of $\mathrm{Al_{0.44}Ga_{0.56}As}$ forming the bottom barrier. This is followed by deposition of 3.5 nm of GaAs. Due to the difference in migration rates of Ga and Al, GaAs redistributes towards the bottom of the nanohole. Such "in-filling" of the nanoholes results in formation of inverted QDs. Finally the dots are capped by a 112 nm $\mathrm{Al_{0.33}Ga_{0.67}As}$ top barrier and 20 nm GaAs layer.

Supplementary Note 2. EXPERIMENTAL TECHNIQUES.

A. Experimental setup.

Experiments were conducted on a home-built cryogenic photoluminescence microscope. A schematic sketch is shown in Supplementary Fig. 1a: the setup is based on a liquid-helium bath cryostat equipped with a 52 mm bore 10 T superconducting magnet producing vertical field (along z axis). A stainless steel insert tube filled with low-pressure exchange helium gas is immersed into liquid helium. The microscope assembly including objective lens, NMR coil and the sample mounted on the nano-positioners is located at the bottom part of the insert, approximately in the middle of the magnet. Free-space optical access is provided via a quartz window at the top of the insert, while electric connection for the NMR coil is achieved with a non-magnetic coaxial cable terminated with an SMA vacuum connector at the insert top.

The detailed schematics of the microscope assembly are shown in two vertical plane projections in Supplementary Figs. 1b and c. The objective lens and NMR coil are fixed in the insert. The objective is a single aspheric lens with a working distance of ∼2 mm and NA of ∼0.55. The NMR coil consists of 8 turns of an enameled copper wire (wire diameter 0.2 mm) wound in 4 layers and produces radiofrequency field along the x axis. The external radius of the coil is smaller than the working distance of the lens used to excite and collect photoluminescence. As a result the coil can be positioned very close to the edge of the quantum dot sample: the distance between the coil edge and the lens focal point is $\sim$0.5 mm.

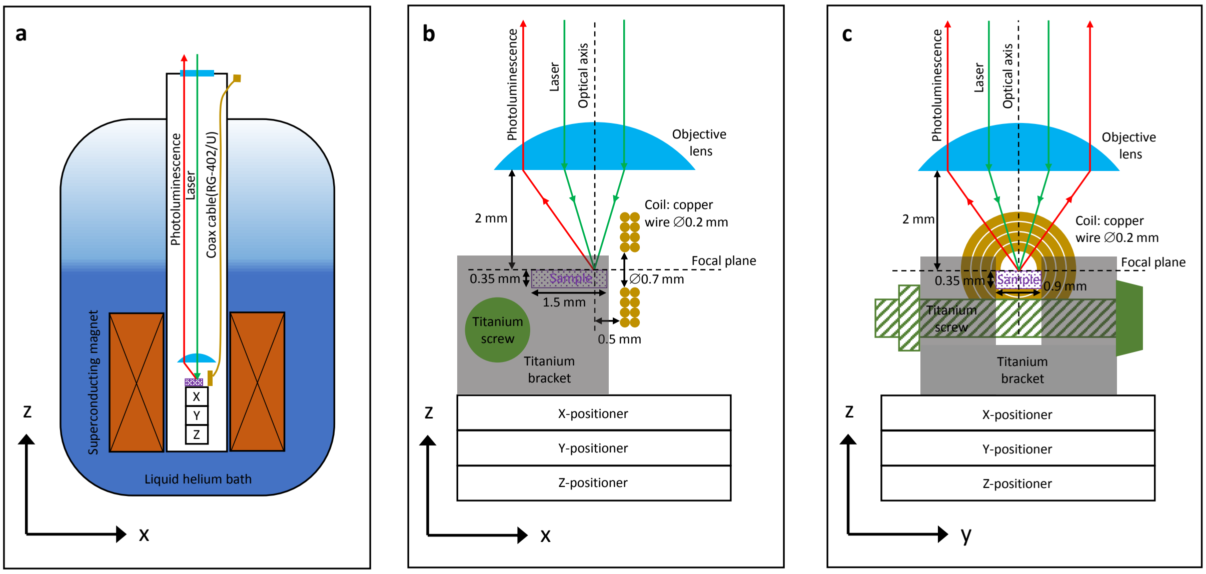

Supplementary Figure 1. **Experimental setup.** **a,** Overall schematic of the cryogenic microscope system used for optically detected NMR. Key components including objective lens, NMR coil, sample, and nano-positioners are shown. **b, c,** Close up schematic drawings of the microscope assembly in two different planes. The drawings are generally not to scale, key dimensions are shown by the arrows with labels. See details in text.

The sample assembly is mounted on an XYZ piezo nano-positioner allowing the sample surface to be scanned and different individual quantum dots to be studied. The sample dimensions are $0.9 \times 1.5 \times 0.35$ mm. The sample is glued in between the "jaws" of a titanium bracket with a U-shaped cross-section. A titanium screw with a nut are used to squeeze the "jaws" of the bracket and exert uniaxial (along y axis) stress on the quantum dot sample. The sample is positioned at the top of the bracket U-shape enabling good optical access and close to the side edge of the bracket allowing proximity to the NMR coil. In order to make the structure symmetric with respect to the yz plane another "dummy" sample of the same size is glued into the bracket at the opposite top edge of the bracket (not shown). Application of the uniaxial strain allows controlled splitting of the quantum dot NMR lines. In this way variation in quadrupolar splitting ν_Q of ^{75}As up to $\sim$100 kHz can be achieved which exceeds the inhomogeneous broadening of the NMR lines by a factor of $\sim$5, making it sufficient to resolve NMR triplets and measure nuclear spin temperature[2,3].

The crystalographic axes of the studied sample are oriented in the following manner: [100] along the z axis (static magnetic field and light propagation), [110] along the x axis (radiofrequency magnetic field), $[1\bar{1}0]$ along the y axis (uniaxial stress).

B. Optical detection of the hyperfine shifts.

In all nuclear spin cooling experiments we use *Optical cooling - rf depolarization - Optical readout* protocol which has been described in detail previously[4–8]. The time diagram of such a measurement is shown in Supplementary Fig. 2

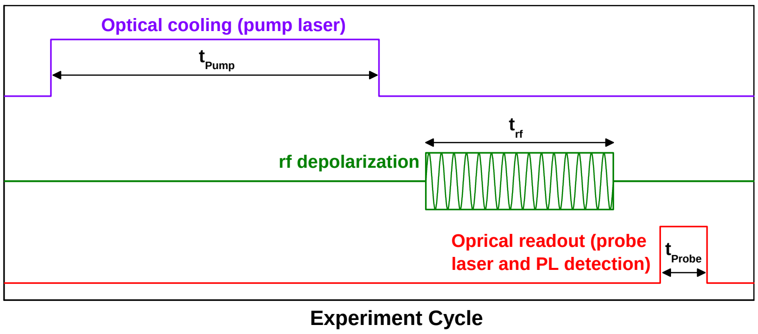

Supplementary Figure 2. **Time diagram of the nuclear spin temperature measurement via selective rf depolarization.** See detailed explanation in Supplementary Note 2 B.

Optical cooling is achieved by pumping with Ti:Sap laser emission of a variable wavelength and power. The largest nuclear spin polarization $|P_{\rm N}| \approx 80$ % is achieved at excitation power of ~ 3000 μW and photon energy of $\sim$1.63 eV for quantum dots emitting at $\sim$1.58 eV and at a photon energy of $\sim$1.645 eV for quantum dots emitting at $\sim$1.63 eV (see further discussion in Supplementary Note 3). The duration of the optical pump is typically $t_{\rm Pump} = 10 - 12$ s, sufficiently long to induce a steady state nuclear spin polarization. A combination of a half-wave and a quarter-wave plates is used to control the degree of circular polarization of the pump laser from -1 to +1 (polarization is varied from σ^- to σ^+ through intermediate elliptical polarizations): in this way the nuclear spin polarization degree could be controlled gradually between its maximum negative and positive values as shown in Fig. 3c of the main text.

Selective depolarization of the nuclei is achieved by applying radiofrequency (rf) oscillating magnetic field with rectangular spectral profile as shown in Fig. 2b of the main text. Such rectangular bands are constructed from frequency combs with comb spacing $f_{\rm MS} = 125$ Hz much smaller than the homogeneous NMR linewidths, so that the combs are equivalent to white noise[8]. The amplitude of the rf field is kept low so that the system is well below the regime of coherent Rabi oscillations and the resulting decay of the nuclear spin polarization is exponential. In such a regime the decay time $\tau_{\rm rf}$ is inverse proportional to the squared amplitude of the rf magnetic field. Typical rf-induced decay times in our experiments are $\tau_{\rm rf} \sim 0.15$ s which corresponds to the amplitude spectral density of the rotating component of the rf field of $\beta_1 \sim 100$ nT/$\sqrt{\mathrm{Hz}}$ (i.e. the amplitude of each mode of the frequency comb is B_1 $\sim$1 μT). The typical duration of the rf pulse in our experiments is $t_{\mathrm{rf}} = 1$ s, significantly longer than τ_{rf} to ensure complete saturation of the chosen NMR transition. We note that the nuclear spin temperature measurements are possible for a wide range of rf amplitudes: it is only required that $T_2 \ll \tau_{\mathrm{rf}} \ll T_1$, where longitudinal and transverse nuclear spin relaxation times are $T_1 \gtrsim 500$ s (Ref.[9]) and $T_2 \lesssim 5$ ms (Ref.[7]) respectively.

After rf depolarization, a HeNe (632.8 nm) probe laser pulse is used to excite quantum dot photoluminescence (PL). The duration of this readout probe pulse is typically $t_{\mathrm{Probe}} = 40 - 100$ ms and is chosen short enough to minimize its effect on the nuclear spin polarization. Example probe PL spectra are shown in Supplementary Fig. 3.

For the neutral dots studied in this work in presence of large magnetic field along the growth axis, the PL spectra measured at low optical powers exhibit emission of all four excitonic states formed by an electron with spin up or down ($\uparrow$, $\downarrow$) and a hole with spin up or down ($\Uparrow$, $\Downarrow$): there are two bright excitons $|\Uparrow\downarrow\rangle$, $|\Downarrow\uparrow\rangle$ and two dark excitons $|\Uparrow\uparrow\rangle$, $|\Downarrow\downarrow\rangle$ that have finite admixture from bright states making them visible in PL[10]. Due to the hyperfine interaction, nuclear spin polarization shifts the energy of each exciton state according to its electron spin and hole spin directions. The contribution of the hole hyperfine interaction is small but not negligible[5]. In order to exclude it and measure pure electron hyperfine shifts, we use the splitting in energies of a bright and a dark exciton with the same hole spin projection, for example a $|\Uparrow\uparrow\rangle$-$|\Uparrow\downarrow\rangle$ pair of states. Such splitting equals the total electron hyperfine shift E_{hf} plus a constant Zeeman splitting determined by the electron and hole g-factors. In order to eliminate the Zeeman contribution and obtain the absolute value of the hyperfine shift for a selected NMR transition of a selected isotope we perform a differential measurement: The probe spectra are measured with rf depolarization (dashed lines in Supplementary Fig. 3) and without (solid lines in Supplementary Fig. 3), the difference in the dark-bright splitting of the two spectra gives the required hyperfine shift. For example the total hyperfine shift E_{hf} of an isotope is found as $E_{\mathrm{hf}} = -\Delta E_{\mathrm{hf}}^{-I\leftrightarrow+I}$, where $\Delta E_{\mathrm{hf}}^{-I\leftrightarrow+I}$ is the change in dark-bright exciton splitting induced by saturating all NMR transitions (see main text and Methods).

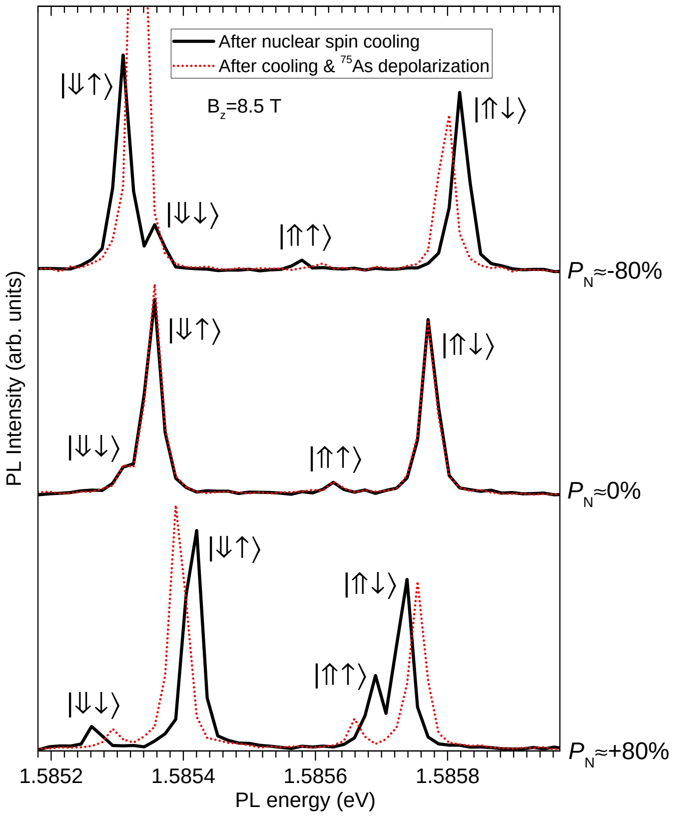

Supplementary Figure 3. **Optical detection of the hyperfine shifts.** Photoluminescence (PL) spectra of a single neutral GaAs/AlGaAs nanohole filled quantum dot in magnetic field $B_z \approx 8.5$ T recorded after cooling the quantum dot nuclear spins to different polarization degrees $P_{\rm N}$ (solid lines). The dashed lines show PL spectra recorded after cooling followed by selective depolarization of the ^{75}As nuclei. In each spectrum four PL lines are observed corresponding to all possible combinations of the electron spin states ($\uparrow$, $\downarrow$) and hole states ($\Uparrow$, $\Downarrow$) forming two bright excitons $|\Uparrow\downarrow\rangle$, $|\Downarrow\uparrow\rangle$ and two dark excitons $|\Uparrow\uparrow\rangle$, $|\Downarrow\downarrow\rangle$ that have finite admixture of bright states making dark states visible in PL[10–12]. The splitting of the $|\Downarrow\uparrow\rangle$-$|\Downarrow\downarrow\rangle$ exciton pair (or the $|\Uparrow\uparrow\rangle$-$|\Uparrow\downarrow\rangle$ pair) depends on the nuclear spin polarization. The change in this splitting induced by rf depolarization yields the electron hyperfine shift $E_{\rm hf}$ of the corresponding isotope (^{75}As in this case). At certain levels of nuclear polarization dark and bright states overlap and anticross (e.g. $|\Downarrow\uparrow\rangle$-$|\Downarrow\downarrow\rangle$ at large negative $P_{\rm N}$ or $|\Uparrow\uparrow\rangle$-$|\Uparrow\downarrow\rangle$ at large positive $P_{\rm N}$), in such cases the other dark-bright pair can still be used to measure $E_{\rm hf}$.

Supplementary Note 3. DEPENDENCE OF THE NUCLEAR SPIN COOLING EFFICIENCY ON THE POWER AND WAVELENGTH OF THE OPTICAL PUMPING.

Supplementary Figure 4a shows a broad-range photoluminescence (PL) spectrum of a studied sample measured under non-resonant laser excitation (at 632.8 nm). Several emission features are observed and ascribed to (from left to right) bulk GaAs substrate, long-wavelength quantum dots (type A), short-wavelength quantum dots (type B) and a wetting layer quantum well (QW). Supplementary Figure 4b shows the total optically induced hyperfine shift E_{hf} and the corresponding nuclear spin polarization degree P_{N} detected on one of the dots type A (marked by an arrow in Supplementary Figure 4a) as a function of a photon energy of a circularly polarized laser at three different excitation powers.

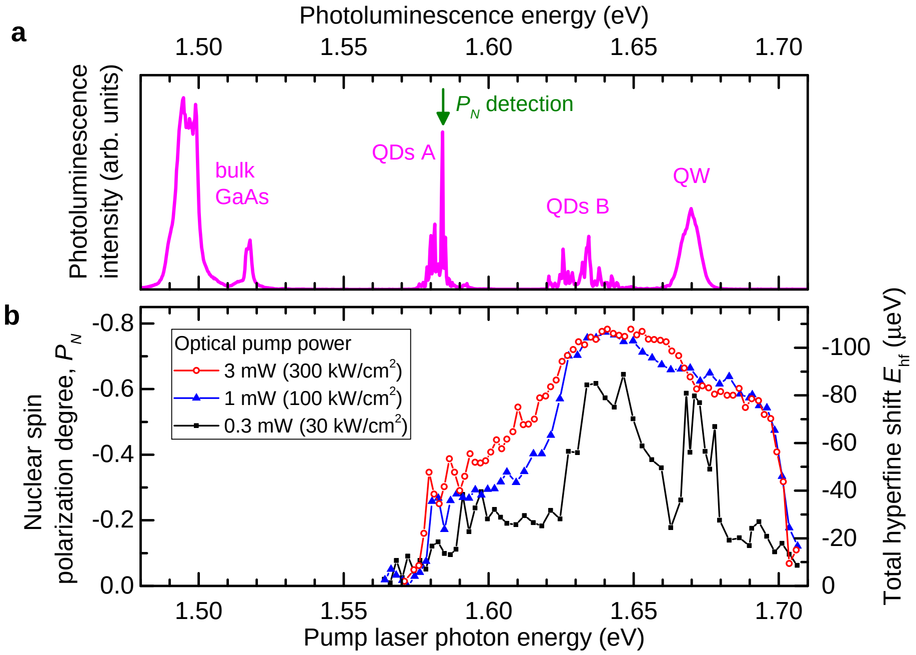

Supplementary Figure 4. **Dependence of the nuclear spin cooling efficiency on the power and wavelength of the optical pumping. a,** Photoluminescence (PL) spectrum measured at $B_z = 5$ T and HeNe laser excitation (632.8 nm). Emission from GaAs substrate, long-wavelength quantum dots (type A), short-wavelength quantum dots (type B) and quantum well (QW) are observed. **b,** Total optically induced hyperfine shift E_{hf} and the corresponding nuclear spin polarization degree P_{N} measured on one of the dots type A (marked by an arrow) as a function of optical pumping photon energy at different optical powers of a circularly polarized laser excitation. The optical power density is calculated assuming the laser spot area of 1 μm^2.

For the lowest used power of 0.3 mW (corresponding to the surface power density of ~30 kW/cm^2) the result is similar to what was observed previously in the same structure[9] at a comparable excitation power of 0.5 mW: two broad peaks in nuclear spin polarization degree P_{N} detected in a type A dot are attributed to the resonant optical pumping of the type B dots (~1.645 eV peak), and the quantum well (~1.675 eV peak consisting of sharp features). When the power is increased up to 3 mW, nuclear spin cooling becomes more efficient for the entire range of the laser photon energies and the broad peaks observed at 0.3 mW broaden further and smear out completely. The largest

$|P_\mathrm{N}|$ is observed for a range of energies approximately corresponding to optical excitation of the type B dots. We thus argue that in the studied structures, the most efficient nuclear spin pumping mechanism is via resonant optical injection of spin polarized excitons into the high-energy type B dots with a subsequent tunneling and relaxation into the low-energy type A dots. Measurements at the laser energy of ~1.63 eV (which is optimal at 3 mW power) for even higher optical powers up to 15 mW (not shown here) have revealed reduction in $|P_\mathrm{N}|$, most likely arising from local sample heating. It also follows from Supplementary Figure 4 that for high power optical pumping, a significant nuclear spin cooling can be induced for the entire range of energies between QDs type A and type B, i.e. resonant excitation of type B dots or QW are not the only mechanisms. We further note that $|P_\mathrm{N}|$ up to 30% is observed when pumping with energies as low as ~5 meV *below* the ground state neutral exciton energy of the studied dot. This may be due to the nuclear spin cooling via optical pumping of bi-exciton, multi-exciton or (multi-)charged states. These observations suggest that optical nuclear spin cooling is a complex process, driven by a combination of various nuclear spin pumping and nuclear spin depolarization mechanisms.

It is thus evident that a significant further effort is required in order to understand the mechanisms and engineer the approaches for achieving even deeper cooling of the nuclear spins with $|P_\mathrm{N}| > 80\%$. In this respect, we note that the data presented in Supplementary Figure 4b provides only a snapshot of the nuclear spin cooling phenomena in the studied dots. Indeed the measurements were conducted with a relatively broad laser excitation (~4 GHz) and coarse steps in photon energy, so that the nuclear spin cooling mechanisms via resonant[13,14] and quasi-resonant (p-shell)[15] optical excitation are yet to be explored. Since each point in Supplementary Figure 4b requires several minutes of PL spectrum integration, a detailed high resolution exploration of $|P_\mathrm{N}|$ as a function of laser power and photon energy (or even more detailed measurements with two or more single-mode tuneable lasers) would require significant experimental effort and is a subject of further work.

Supplementary Note 4. DERIVATION OF ELECTRON HYPERFINE CONSTANTS A: DETAILED ANALYSIS.

The experimentally measured hyperfine shift E_hf induced by the polarized nuclear spins is defined as the change in the energy splitting of the $S_\mathrm{z} = \pm 1/2$ electron spin levels. The total hyperfine shift is a sum of the hyperfine shifts induced by different isotopes i:

$$E_{\mathrm{hf}} = \sum_i E^i_{\mathrm{hf}}, \tag{1}$$

The hyperfine shift of the i-th isotope in a quantum dot is given by

$$E^i_{\mathrm{hf}} = A^i I^i \sum_j \rho^i x^i(\mathbf{r}_j)|F(\mathbf{r}_j)|^2 P_{\mathrm{N}}(\beta^i(\mathbf{r}_j)), \tag{2}$$

where the summation goes over all cationic or anionic (depending on the type of the isotope i) sites j with coordinates $\mathbf{r}_j$, A^i is the electron hyperfine constant determined only by the fundamental constants and the density of the electron Bloch wavefunction $|\psi(0)|^2$ at the nucleus, I^i is the nuclear spin and ρ^i is the natural abundance of the i-th isotope. The nuclear spin polarization degree P_{N} is always defined and is uniquely related (via Brillouin function) to the dimensionless inverse nuclear spin temperature β if the spin temperature T_{N} exists ($\beta = h\nu_L/k_{\mathrm{b}}T_{\mathrm{N}}$, where ν_L is the nuclear Larmor frequency, and for spin I=3/2 the $P_{\mathrm{N}}(\beta^i)$ is given by the last of Eqs. 5 of the Methods section when divided by $-kAI$). The inverse temperature $\beta^i(\mathbf{r}_j)$ and the mole fraction $x^i(\mathbf{r}_j)$ are not constant in general and depend on $\mathbf{r}_j$. ($x^i(\mathbf{r}_j)$ is defined as the probability that the j-th site is occupied by an atom of the element to which the isotope i belongs, e.g. x=0.5 for Al and Ga in a uniform $\mathrm{Al_{0.5}Ga_{0.5}As}$ alloy). $F(\mathbf{r}_j)$ is the envelope wavefunction of a localized electron state normalized in a way that $\sum_j |F(\mathbf{r}_j)|^2 = 1$ when summed over all cationic or anionic sites of the crystal.

Supplementary Eq. 2 gives a complete description of the experimentally observable hyperfine shifts and is the key expression used in the subsequent analysis. If nuclear spin temperature exists Supplementary Eq. 2 can be readily adjusted to yield the experimentally measurable changes in hyperfine shifts $\Delta E^{m\leftrightarrow m+1}_{\mathrm{hf}}$ and $\Delta E^{m\leftrightarrow m+2}_{\mathrm{hf}}$ induced by selective rf saturation of the NMR transitions, for this $P_{\mathrm{N}}(\beta)$ needs to be substituted by the corresponding hyperbolic function of β (obtained from Eqs. 5 of the Methods by dividing by $-kAI$).

If β^i (and hence P^i_{N}) is constant over the volume of a quantum dot and its vicinity, Supplementary Eq. 2 simplifies to Eq. 1 of the main text [$E^i_{\mathrm{hf}} = kA^iI^iP^i_{\mathrm{N}}$ with k determined only by the structural parameters of the quantum dot ρ^i, $x^i(\mathbf{r}_j)$ and $F(\mathbf{r}_j)$] also leading to Eqs. 5 of the Methods. For the spatially inhomogeneous β^i, Eq. 1 of the main text still describes the experimentally measured hyperfine shifts E^i_{hf} if P^i_{N} is treated as an average polarization degree, with k ($0 \leq k \leq 1$) depending not only on the $x^i(\mathbf{r}_j)$ and $F(\mathbf{r}_j)$ functions, but also on the particular form of $\beta^i(\mathbf{r}_j)$. In a similar way, the experimentally measured $\Delta E^{m\leftrightarrow m+1}_{\mathrm{hf}}$ and $\Delta E^{m\leftrightarrow m+2}_{\mathrm{hf}}$ can be treated as a result of averaging over the dot volume. The crucial difference is that the $\Delta E^{m\leftrightarrow m+1}_{\mathrm{hf}}$($\Delta E^{-I\leftrightarrow +I}_{\mathrm{hf}}$)

and $\Delta E_{\mathrm{hf}}^{m\leftrightarrow m+2}(\Delta E_{\mathrm{hf}}^{-I\leftrightarrow +I})$ dependencies are not necessarily described by Eqs. 5 of the Methods if the hyperfine shifts are obtained by averaging over a distribution of $\beta^i(\mathbf{r}_j)$. Since model fitting of the $\Delta E_{\mathrm{hf}}^{m\leftrightarrow m+1}(\Delta E_{\mathrm{hf}}^{-I\leftrightarrow +I})$ and $\Delta E_{\mathrm{hf}}^{m\leftrightarrow m+2}(\Delta E_{\mathrm{hf}}^{-I\leftrightarrow +I})$ experimental data is required for the derivation of the nuclear spin temperatures and hyperfine constants, additional justification of the analysis is needed and is presented below.

One can see from Supplementary Eq. 2 what the difficulty is: the experimentally measured hyperfine shifts E_{hf}^i [left side of the equation] are scalars and can not on their own give full information on the three-dimensional distributions $\beta^i(\mathbf{r}_j)$, $x^i(\mathbf{r}_j)$ and $F(\mathbf{r}_j)$ [right side of the equation], and thus additional information and/or assumptions about these functions are needed. The detailed analysis is presented in the subsequent subsections and can be outlined as follows: (A) the molar fractions $x^i(\mathbf{r}_j)$ are estimated from the structural studies on GaAs nanohole quantum dots, (B) the electron envelope wavefunctions $F(\mathbf{r}_j)$ are calculated numerically by solving the Schrodinger equation, (C) we show that the particular form of $\beta^i(\mathbf{r}_j)$ is not important and the derivation of the nuclear spin polarization degrees is robust for a wide range of distributions of β^i.

A. Effect of the quantum dot structure $x^i(\mathbf{r}_j)$.

Since arsenic is the only anion in the studied GaAs/AlGaAs structures its molar fraction is $x^{\mathrm{As}} = 1$, simplifying Eq. 2. As to cations (gallium and aluminium), the earlier TEM studies on similar sample structures have shown sharp interfaces between GaAs and AlGaAs layers[16]. We thus use the known molar fractions of aluminium in the barriers to model $x^i(\mathbf{r}_j)$ as a piece-wise function. Such approximation is further justified *a posteriori* by the smallness ($< 12\%$) of the fraction of the electron wavefunction in the AlGaAs layers as confirmed by wavefunction calculations (see below in B). Under such conditions, the average cationic molar fractions probed by the electron are effectively $x^{\mathrm{Ga}} \approx 1$, $x^{\mathrm{Al}} \approx 0$ and the particulars of Al/Ga intermixing profile have little effect on the hyperfine shifts and the derivation of the nuclear spin temperatures.

B. Calculation of the electron envelope wavefunction $F(\mathbf{r}_j)$.

The electron envelope wavefunction $F(\mathbf{r}_j)$ that appears as a weighting function in Eq. 2 is calculated by solving the Schrodinger equation using effective mass approximation. We generally follow the approach described in Ref.[17]. The electron mass is taken to be m_{e} =$(0.067+0.083x^{\mathrm{Al}})m_0$, and heavy-hole anisotropic masses are taken to be $m_{\mathrm{hh,z}}$ =$(0.33+0.18x^{\mathrm{Al}})m_0$, $m_{\mathrm{hh,xy}}$ =$(0.11+0.10x^{\mathrm{Al}})m_0$, where m_0 is the free electron mass. The energy discontinuities at the GaAs/Al$_x$Ga$_{1-x}$As interface are taken to be $0.79x^{\mathrm{Al}}$ eV for the conduction band and $0.51x^{\mathrm{Al}}$ eV for the valence band respectively. We solve single-particle equations for the electron and the hole separately and the contribution of the Coulomb interaction to the exciton energy is calculated as a perturbation.

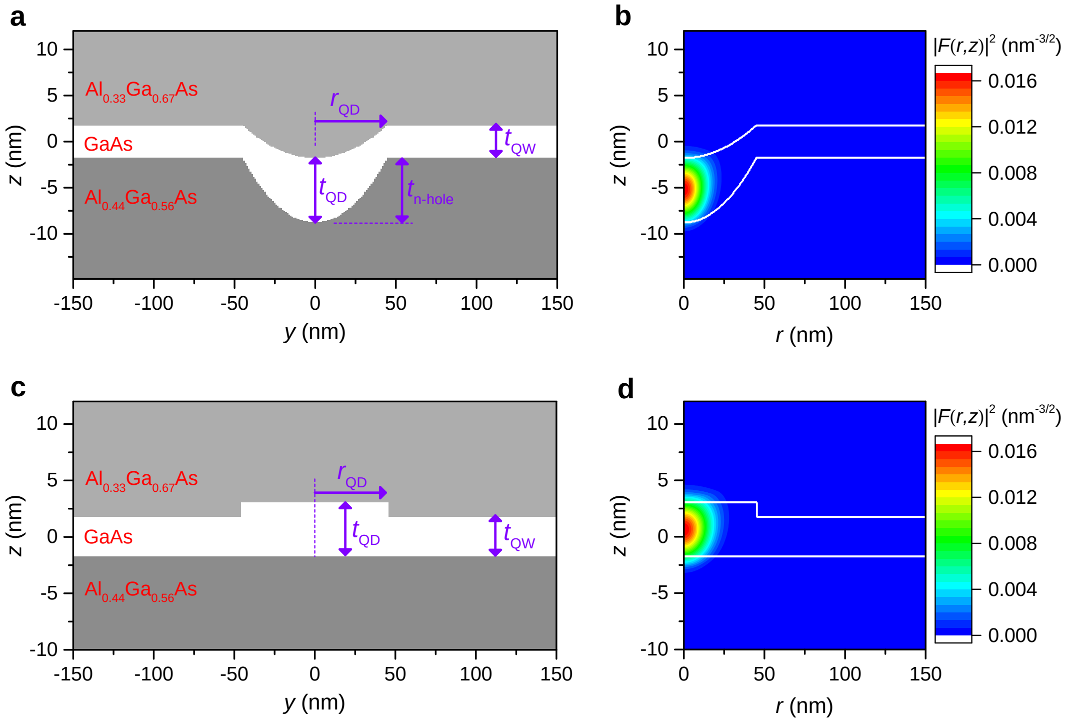

Supplementary Figure 5. **Model quantum dot structures and calculated electron envelope wavefunctions.** **a,** Cross-section of a model structure of a nanohole GaAs/GaAs quantum dot. Cylindrical symmetry over z axis is assumed. The geometry of the structure is determined by quantum well thickness (t_{QW}), quantum dot thickness (t_{QD}), nanohole depth ($t_{\text{n-hole}}$), and quantum dot radius (r_{QD}). **b,** Calculated electron wavefunction profile in cylindrical coordinates for the dot structure in (**a**). White lines show the GaAs/AlGaAs boundaries. **c,** Cross-section of a disk-shaped thickness fluctuation quantum dot. **d,** Calculated electron wavefunction profile in cylindrical coordinates for the dot structure in (**c**).

Quantum dots formed by nanohole etching and infilling are modeled using the structure with a cross-section shown in Supplementary Fig. 5a. We assume cylindric symmetry which simplifies the problem. The aluminium molar fractions in the barriers and the thickness of the GaAs quantum well (QW) are taken according to the growth protocol. The calculated QW exciton transition energy is found to match the experimental value of ~ 1.665 eV (see Supplementary Fig. 4a) for $t_{\mathrm{QW}} = 3.55$ nm in very good agreement with the design QW thickness of $t_{\mathrm{QW}} = 3.5$ nm. The depth of the nanohole ($t_{\text{n-hole}}$=7.0 nm) the radius of the dot (r_{QD}=45.0 nm), and the thickness of the dot

(t_{QD}=7.0 nm) are taken to be comparable to the results of the AFM studies on similar structures[1]. The electron wavefunction calculated for such structure is shown in Supplementary Fig. 5b, the optical transition energy is found to be ∼1.585 eV in good agreement with the emission energies of the long-wavelength (type A) dots.

Short-wavelength quantum dots (type B) were previously shown to arise from the irregularities in GaAs layer thickness at the rims of the nanoholes[9]. As a simple approximation we model such dots as disk-shaped QW thickness fluctuations as shown in Supplementary Fig. 5c. With r_{QD}=45.0 nm and t_{QD}=4.81 nm we find transition energy of ∼1.625 eV in good agreement with experiment. The corresponding electron wavefunction profile is shown in Supplementary Fig. 5d.

We have performed calculations for a wide range of quantum dot dimensions t_{QD}, r_{QD}, $t_{\text{n-hole}}$. As expected, we find that the same E_{PL} can be obtained for an infinite number of different combinations of t_{QD}, r_{QD}, $t_{\text{n-hole}}$: the exciton optical transition energy alone does not reveal the entire quantum dot structure. On the other hand, as we show below, the precise knowledge of the electron wavefunction $F(r,z)$ is not required for the calculations of the hyperfine shifts (based on Supplementary Eq. 2). It is sufficient to know the integral properties of $F(r,z)$ such as the fractions of the wavefunction density within the quantum dot GaAs layer and the AlGaAs barriers. These wavefunction density fractions W are shown in Supplementary Fig. 6a by the symbols as a function of the exciton transition energy E_{PL} calculated for a large number of model quantum dot structures with different dimensions (both nanohole and disk-shaped dots are included). It can be seen that the calculated points reveal clear $W(E_{\mathrm{PL}})$ dependencies: thus using the experimental E_{PL} energy derived from a PL spectrum (such as shown in Supplementary Fig. 6a by the line) and the calculated $W(E_{\mathrm{PL}})$ one can estimate the wavefunction fractions W in the QD and barrier layers for a given studied quantum dot. Since the W values are the functions of E_{PL} only, it is not required to know the exact QD shape and size, instead it is sufficient to choose some realistic QD model structure that yields E_{PL} matching the experimental value. In the following analysis we use the particular dot model structures of Supplementary Fig. 5a and 5c whose E_{PL} fit the experimentally observed values of the long- and short-wavelength dots respectively.

C. The role of the nuclear spin polarization inhomogeneity $\beta^i(\mathbf{r}_j)$.

With $x^i(\mathbf{r}_j)$ and $F(\mathbf{r}_j)$ estimated above, it is the spatial distribution of the polarization degree $P^i_{\mathrm{N}}(\mathbf{r}_j)$ [or equivalently the distribution of the inverse nuclear spin temperature $\beta^i(\mathbf{r}_j)$] that needs to be found in order to be able to use Supplementary Eq. 2 to calculate the measured hyperfine

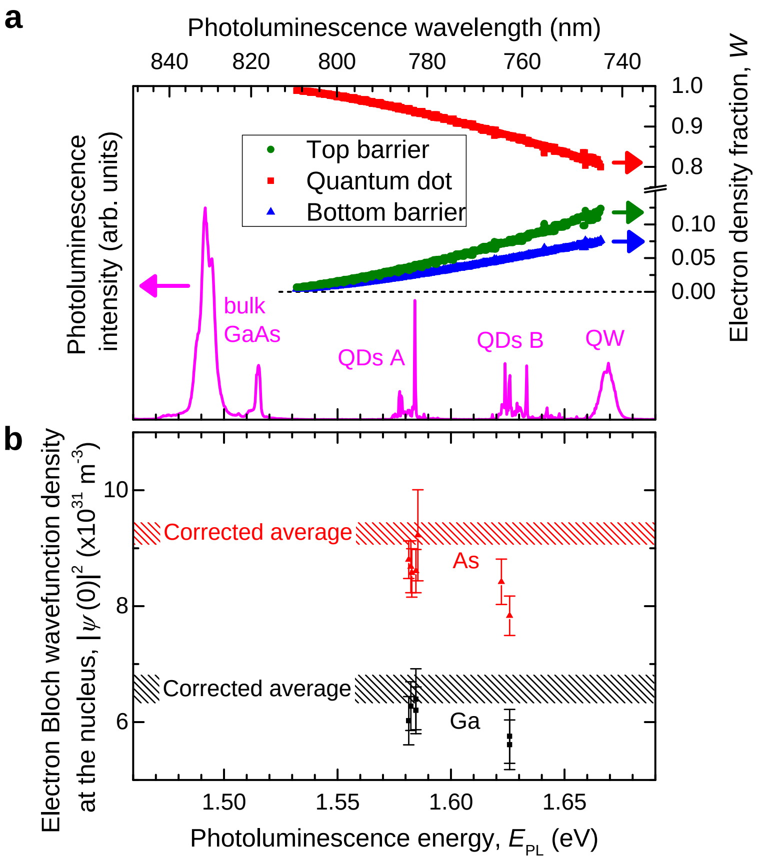

Supplementary Figure 6. **Electron wavefunction in the nano-hole GaAs/AlGaAs quantum dots.** **a,** Typical experimental photoluminescence spectrum of the studied sample (left scale) and the fraction of the electron envelope wavefunction density in the QD and barrier layers as a function of the optical transition energy (right scale) derived from model calculations. **b,** Electron Bloch wavefunction density at the nucleus $|\psi(0)|^2$. Each symbol corresponds to $|\psi(0)|^2$ derived from experimental selective rf depolarization of the nuclear spins in an individual quantum dot. The $|\psi(0)|^2$ values are derived from Eq. 4 of the main text based on the hyperfine constants derived in turn from the fitting of the experimental results such as shown in Figs. 3a, b of the main text. In such fits we assume uniform nuclear polarization in quantum dots $P^i_{\mathrm{N}}(\mathbf{r}_j)$ =const. The results are shown for Ga (squares) and As (triangles) nuclei with respect to the ground state exciton luminescence of each quantum dot E_{PL} with error bars corresponding to 95% confidence level. By taking into account the non-uniformity of $P^i_{\mathrm{N}}(\mathbf{r}_j)$ as described in Supplementary Note 4 C, we calculate the corrected $|\psi_{\mathrm{As}}(0)|^2$=(9.25±0.20)×10^{31} m^{-3} and $|\psi_{\mathrm{Ga}}(0)|^2$=(6.57±0.25)×10^{31} m^{-3} averaged over all studied dots as shown by dashed areas representing 95% confidence level estimates.

shifts. Due to the complex electron-nuclear spin dynamics, experimental measurement or the first principle modeling of $P^i_{\mathrm{N}}(\mathbf{r}_j)$ distribution in a quantum dot is far beyond what can be achieved at present. Yet, as we now show, it is possible to construct a model for $P^i_{\mathrm{N}}(\mathbf{r}_j)$ that is sufficiently good to derive electron hyperfine constants A from experimental data.

We start by noting that $P_{\mathrm{N}}^{i}(\mathbf{r}_j)$ should reach its maximum near the center of the dot ($|\mathbf{r}| \approx 0$) where the electron density peaks and the probability of the electron-nuclear spin flip-flop is maximized. With increasing $|\mathbf{r}|$ the polarization $P_{\mathrm{N}}^{i}(\mathbf{r}_j)$ should decay monotonically towards 0, since the nuclei remain unpolarized away from the dot. Now let us suppose that the nuclear spins are initially unpolarized in the entire sample ($P_{\mathrm{N}} \approx 0$) and that the optical cooling is introduced at time $t = 0$. At small t the resulting $P_{\mathrm{N}}^{i}(\mathbf{r}_j)$ will be proportional to the nuclear spin cooling rate at each point $\mathbf{r}_j$. This rate in turn is proportional to the electron envelope wavefunction density $|F(\mathbf{r}_j)|^2$ controlling the electron-nuclear flip-flop rate, hence $P_{\mathrm{N}}^{i}(\mathbf{r}_j) \propto |F(\mathbf{r}_j)|^2$ is expected for short t. At longer times t, nuclear spin diffusion[18,19] will act to establish a more uniform spatial distribution of $P_{\mathrm{N}}^{i}(\mathbf{r}_j)$ in the quantum dot and its vicinity. If the longitudinal nuclear spin relaxation was absent, spin diffusion would eventually generate uniform P_{N}^{i} =const independent of $\mathbf{r}_j$ for $t \to \infty$. In the real quantum dots in the studied sample the longitudinal relaxation times are long (T_1 >500 s) but not infinite[9]. We thus conclude that the real $P_{\mathrm{N}}^{i}(\mathbf{r}_j)$ produced by optical cooling in the studied GaAs/AlGaAs quantum dots is between the two limiting cases of $P_{\mathrm{N}}^{i}(\mathbf{r}_j)$ =const and $P_{\mathrm{N}}^{i}(\mathbf{r}_j) \propto |F(\mathbf{r}_j)|^2$.

Let us first consider a uniform nuclear spin polarization $P_{\mathrm{N}}^{i}(\mathbf{r}_j)$ =const. In this case, the sum in the Supplementary Eq. 2 becomes a constant k determined only by the structure of the quantum dot, in particular $k = 1$ if ^{75}As nuclei ($x = \rho = 1$) are considered. Under these assumptions we can use Eqs. 5 of the Methods to fit the experimental data and derive the nuclear spin temperatures and hyperfine constants A^i. The densities of the electron Bloch wavefunction at the nucleus $|\psi(0)|^2$ calculated from the fitted values of A^i (see Eq. 4 of the main text) are shown in Supplementary Fig. 6b by the symbols for all studied quantum dots against their photoluminescence energy E_{PL}. For all studied quantum dots we find that the assumption of $P_{\mathrm{N}}^{i}(\mathbf{r}_j)$ =const leads to good agreement between experiment and fitting, such as shown in Figs. 3a, b of the main text. On the other hand, there is a small but distinct difference in the fitted $|\psi(0)|^2$ values between the long-wavelength (type A) and short-wavelength (type B) quantum dots. As it follows from Supplementary Fig. 6b, the experiments on type B dots that have larger fraction of the electron density in the barriers, give underestimated values of A^i and $|\psi(0)|^2$. This is a clear sign that the $P_{\mathrm{N}}^{i}(\mathbf{r}_j)$ =const approximation is not exact, and that the deviation arises from the reduced polarization degree $|P_{\mathrm{N}}^{i}|$ in the barriers.

We now examine the opposite case of the largest possible inhomogeneity of the nuclear spin polarization. For this we consider the model structure of Supplementary Fig. 5a with electron envelope wavefunction shown in Supplementary Fig. 5b, and substitute $P_{\mathrm{N}}^{i}(\mathbf{r}_j) \propto |F(\mathbf{r}_j)|^2$ in Supplementary Eq. 2 allowing the hyperfine shifts to be calculated. In order to make the analysis

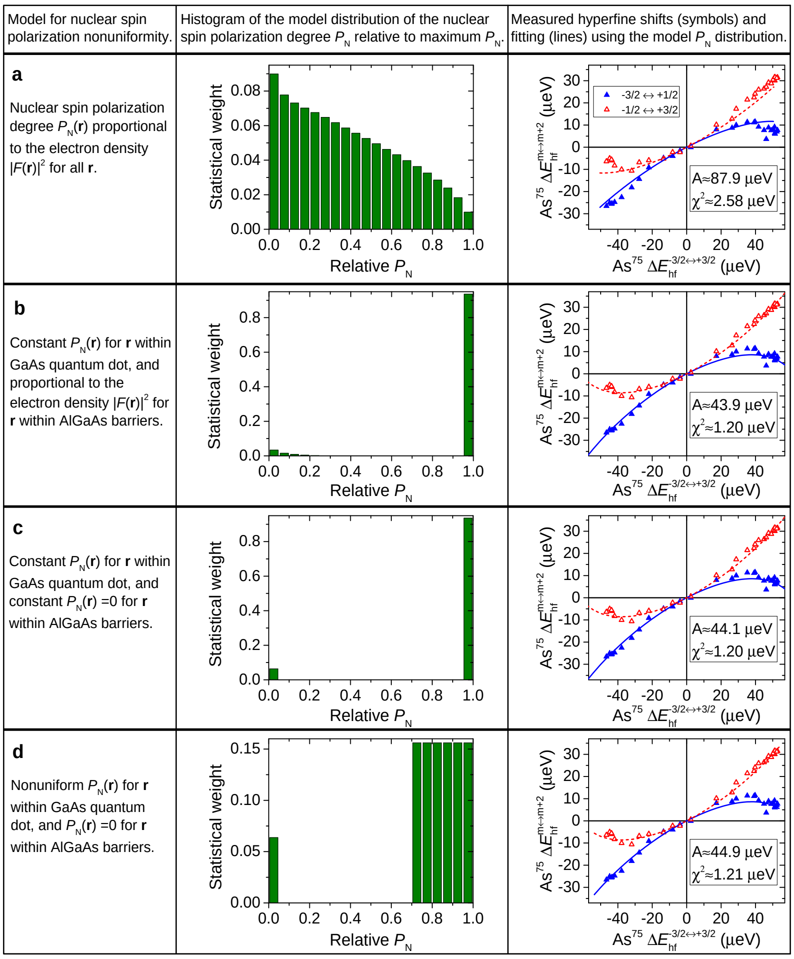

Model for nuclear spin polarization nonuniformity.

Histogram of the model distribution of the nuclear spin polarization degree P_N relative to maximum P_N.

Measured hyperfine shifts (symbols) and fitting (lines) using the model P_N distribution.

a Nuclear spin polarization degree $P_N(\mathbf{r})$ proportional to the electron density $|F(\mathbf{r})|^2$ for all $\mathbf{r}$.

b Constant $P_N(\mathbf{r})$ for $\mathbf{r}$ within GaAs quantum dot, and proportional to the electron density $|F(\mathbf{r})|^2$ for $\mathbf{r}$ within AlGaAs barriers.

c Constant $P_N(\mathbf{r})$ for $\mathbf{r}$ within GaAs quantum dot, and constant $P_N(\mathbf{r})$ =0 for $\mathbf{r}$ within AlGaAs barriers.

d Nonuniform $P_N(\mathbf{r})$ for $\mathbf{r}$ within GaAs quantum dot, and $P_N(\mathbf{r})$ =0 for $\mathbf{r}$ within AlGaAs barriers.

Supplementary Figure 7. **Derivation of the nuclear spin temperature and hyperfine constants taking into account spatially inhomogeneous nuclear spin polarization P_N.** Rows **a-d** show results for different model distributions of P_N^i (left column). Middle column: histograms of the P_N^i distributions within the electron wavefunction volume. Right column: hyperfine shifts $\Delta E_\mathrm{hf}^{m\leftrightarrow m+2}$ induced by selective saturation of two out of the three dipolar NMR transitions of the spin-3/2 ^{75}As nuclei as a function of the hyperfine shift $\Delta E_\mathrm{hf}^{-I\leftrightarrow +I}$ resulting from simultaneous saturation of all NMR transitions. Symbols show experiments on an individual quantum dot A1, while lines show model calculations using Supplementary Equation 2 and Eqs. 5 of the Methods. In calculations the molar fraction of As is x^As=1 and the electron envelope wavefunction $F(\mathbf{r}_j)$ is from Supplementary Fig. 5b. Hyperfine constant A is used as the only fitting parameter and is shown for each calculation together with the root mean square fitting residual χ^2.

more intuitive we build a histogram of the weighted P_N^i values that appear in the sum of the Supplementary Eq. 2. For the case of $P_\mathrm{N}^i(\mathbf{r}_j) \propto |F(\mathbf{r}_j)|^2$ such histogram is shown in the middle column of the Supplementary Fig. 7a (top row) for the As nuclei. Each value on the horizontal axis is the polarization degree P_N^i normalized by its maximum value at the center of the dot, and the height of each bar reflects the fraction of the nuclei with such P_{N}^{i} weighted by the envelope wavefunction density $|F(\mathbf{r}_j)|^2$ and the molar fraction $x(\mathbf{r}_j)$ at such nuclear sites. The right graph of the Supplementary Fig. 7a (top row) shows experimental (symbols) and fitted (lines) dependencies $\Delta E_{\mathrm{hf}}^{m\leftrightarrow m+2}(\Delta E_{\mathrm{hf}}^{-I\leftrightarrow +I})$ for As nuclei in QD A1. The fitting yields an unrealistically large A^{As} $\approx$87.9 μeV with a large RMS fitting residual of $\chi \approx 2.58$ μeV exceeding the experimental error. Thus we can rule out the $P_{\mathrm{N}}^{i}(\mathbf{r}_j) \propto |F(\mathbf{r}_j)|^2$ case.

Combining the above observations, we conclude that the real profile of the nuclear spin polarization degree $P_{\mathrm{N}}^{i}(\mathbf{r}_j)$ is much closer to the limiting case of a constant value, rather than to the opposite limit of strongly inhomogeneous $P_{\mathrm{N}}^{i}(\mathbf{r}_j) \propto |F(\mathbf{r}_j)|^2$. In other words, the spatial width of the $P_{\mathrm{N}}^{i}(\mathbf{r}_j)$ distribution is significantly larger than that of the envelope wavefunction density $|F(\mathbf{r}_j)|^2$. On the other hand, $P_{\mathrm{N}}^{i}(\mathbf{r}_j)$ is not exactly constant, most likely due to the reduced $|P_{\mathrm{N}}^{i}|$ in the AlGaAs barriers. We now discuss how this residual spatial inhomogeneity of $P_{\mathrm{N}}^{i}(\mathbf{r}_j)$ can be accounted for in order to improve the accuracy of the hyperfine constant measurement.

Let us assume that optical cooling produces constant P_{N}^{i} within the quantum dot layer, while outside the dot the polarization degree scales as $P_{\mathrm{N}}^{i}(\mathbf{r}_j) \propto |F(\mathbf{r}_j)|^2$. The corresponding histogram of P_{N}^{i} and fitted $\Delta E_{\mathrm{hf}}^{m\leftrightarrow m+2}(\Delta E_{\mathrm{hf}}^{-I\leftrightarrow +I})$ dependencies are shown in Supplementary Fig. 7b (second row from the top). Such a model for $P_{\mathrm{N}}^{i}(\mathbf{r}_j)$ gives an accurate fit with an RMS residual of $\chi \approx 1.20$ μeV within the experimental error of the electron hyperfine shift measurements. The assumption of a constant level of P_{N}^{i} within the dot volume can be well justified: long optical cooling times (> 10 s) used in our experiments give sufficient time for nuclear spin polarization to be redistributed via spin diffusion. On the other hand the reduction of P_{N}^{i} in AlGaAs barriers can be understood to arise from the quadrupolar induced suppression of the spin diffusion at the GaAs/AlGaAs interfaces[9,20].

Very similar fitted value of the hyperfine constant A is obtained if we assume a simple bimodal distribution for P_{N}^{i} (constant P_{N}^{i} within the dot and $P_{\mathrm{N}}^{i} = 0$ in the barriers as shown in Supplementary Fig. 7c, third row from the top). It is thus evident that the detailed form of $P_{\mathrm{N}}^{i}(\mathbf{r}_j)$ distribution in the barriers is not critical due to the small overall effect of the barrier nuclear spin polarization. Importantly, when we perform fitting with bimodal distributions of Supplementary Figs. 7b,c we obtain very close values of the hyperfine constant A (and hence $|\psi(0)|^2$) for both type A and type B dots – this is a good indication that bimodal distribution of P_{N}^{i} is a good approximation to the real distribution of the optically induced $P_{\mathrm{N}}^{i}(\mathbf{r}_j)$.

We now note that the fitting with a bimodal distribution of Supplementary Fig. 7c is equivalent to fitting with a constant $P_{\mathrm{N}}^{i}(\mathbf{r}_j)$ in the entire sample, but with hyperfine constant A replaced by kA. This is because the nuclei with $P_{\mathrm{N}}^{i} = 0$ do not contribute to the hyperfine shifts $\Delta E_{\mathrm{hf}}^{m\leftrightarrow m+2}$

and $\Delta E_{\mathrm{hf}}^{-I\leftrightarrow+I}$, in which case the additional factor k equals W, where W is the fraction of the electron density in the GaAs QD layer shown in Supplementary Fig. 6a (we consider here the case of ^{75}As where $\rho = x = 1$).

Finally, we examine a case where the barrier nuclei are not polarized ($P_{\mathrm{N}}^{i} = 0$), while the polarization of the QD nuclei is not constant. As an example we use a rectangular distribution with a histogram shown in the middle plot of Supplementary Fig. 7d, where we allow the weighted P_{N}^{i} to be uniformly spread between 70% and 100% of its maximum value, which is likely an exaggeration of the inhomogeneity in a real quantum dot. As the right plot of Supplementary Fig. 7d shows we still find a very good fit with fitted hyperfine constant A similar to that obtained from a bimodal distributions of Supplementary Figs. 7b, c. We also find very similar average polarization degrees P_{N}^{i} derived from the fits with different P_{N}^{i} distributions shown in Supplementary Figs. 7b-d.

We thus summarize with the following conclusions. From the measurements on short- and long-wavelength quantum dots we conclude that P_{N}^{i} is reduced in the barriers, which is explained by the suppression of the nuclear spin diffusion at the GaAs/AlGaAs interfaces[9,20]. Our measurement technique is not very sensitive to the details of the spatial distribution $P_{\mathrm{N}}^{i}(\mathbf{r}_j)$ of the nuclear spin polarization. This however, comes as an advantage, allowing robust measurement of the average P_{N}^{i} and T_{N} within the GaAs QD layer regardless of the details of the $P_{\mathrm{N}}^{i}(\mathbf{r}_j)$ profile. In this Supplementary Note we have presented a detailed first-principles procedure for deriving the electron hyperfine constants A from the NMR experiments taking into account the spatial inhomogeneity of the nuclear spin polarization degree $P_{\mathrm{N}}^{i}(\mathbf{r}_j)$. At the same time we have shown that a simplified analysis assuming $P_{\mathrm{N}}^{i}(\mathbf{r}_j)$ =const (presented in the main text) gives very similar results as long as $P_{\mathrm{N}}^{i}(\mathbf{r}_j)$ distribution satisfies rather generic constraints. The only difference is that instead of the hyperfine constants A, the simplified model fitting yields a scaled kA where the structural factor $k \leq 1$ depends on the electron wavefunction density fraction W within the GaAs quantum dot volume. This fraction W can be estimated by solving the Schrodinger equation for *any* reasonable model structure whose photoluminescence energy E_{PL} matches the experimentally measured E_{PL} – it is not required to know the exact shape and size of the quantum dot. Even if the value of k can not be estimated, the simplified analysis still gives a reliable measure of the average P_{N}^{i} within the dot volume, making the techniques reported here a valuable tool for analysis of the nuclear spin bath thermodynamics in semiconductor quantum dots.

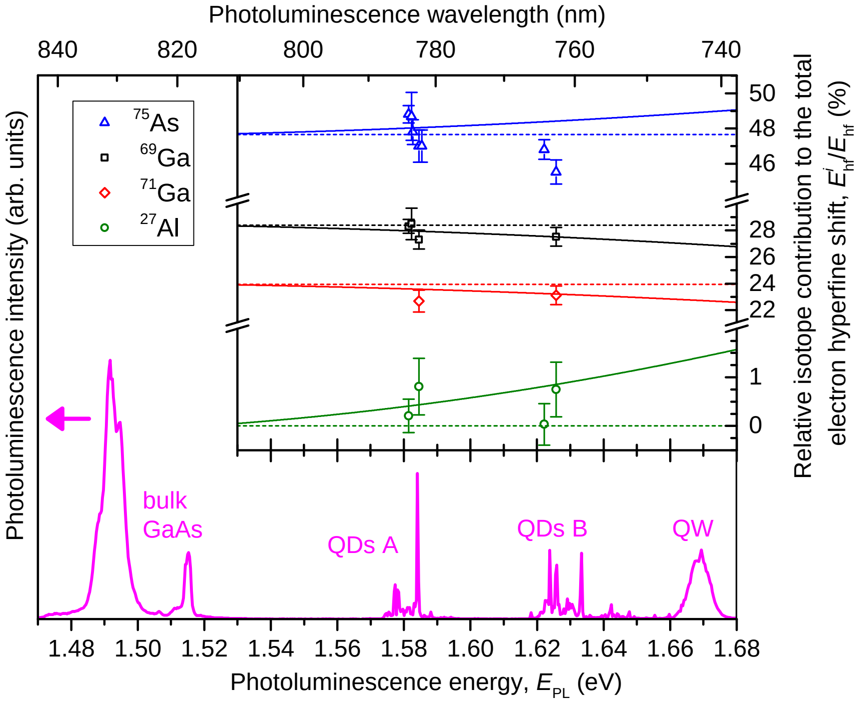

Supplementary Figure 8. **Relative contributions of the isotopes to the optically detected electron hyperfine shift.** Typical experimental photoluminescence spectrum of the studied sample (left scale) and the relative contribution of each isotope $E^i_{\rm hf}$ to the total electron envelope shift $E_{\rm hf}$. Symbols show experimentally measured values with respect to the ground state exciton luminescence of each quantum dot $E_{\rm PL}$ with error bars corresponding to 95% confidence level. Solid lines show calculations for the case of homogeneous nuclear spin polarization $P^i_{\rm N}(\mathbf{r}_j)$ =const, while dashed lines correspond to the case of bimodal distribution with constant $P^i_{\rm N}$ within the dot and $P^i_{\rm N} = 0$ in the barriers.

D. Effect of nuclear spin polarization inhomogeneity on the hyperfine shift of ^{27}Al and other isotopes.

Having discussed how spatial inhomogeneity of the nuclear spin polarization manifests itself in the measurements of the nuclear spin temperature and electron hyperfine constants, it is useful to examine it from a different perspective, by looking at the total hyperfine shifts of different isotopes. In particular, the spin-5/2 ^{27}Al is present in the AlGaAs barriers only, so one may ask if aluminum hyperfine shifts can be used to examine the degree of nuclear spin polarization in the barriers.

The symbols in the inset of Supplementary Fig. 8 show the hyperfine shift $E^i_{\rm hf}$ of each isotope i relative to the total hyperfine shift $E_{\rm hf}$ of all isotope measured in different quantum dots. These values are derived from experiments such as shown in Fig. 3c of the main text. In all studied dots, the contributions of ^{75}As/^{69}Ga/^{71}Ga are approximately split as 48%/28%/23%. Measurements on ^{27}Al consistently reveal non-zero but very small hyperfine shift <1% of the total. We note that due to the smallness of the signal only the total aluminium shift $E_{\mathrm{hf}}^{\mathrm{Al}}$ could be measured (by simultaneously saturating all of its 5 NMR transitions), but no NMR spectroscopy or nuclear spin temperature probing could be performed.

The relative contributions of isotopes are also calculated from Supplementary Eqs. 1, 2 using electron envelope wavefunction fractions W shown in Supplementary Fig. 6. The results are shown in Supplementary Fig. 8 by the solid lines for the case of homogeneous nuclear spin polarization $P_{\mathrm{N}}^{i}(\mathbf{r}_j)$ =const, and by the dashed lines for bimodal distribution with constant P_{N}^{i} within the dot and $P_{\mathrm{N}}^{i} = 0$ in the barriers. In these model calculations we assumed equal polarization degree of all isotopes, which is confirmed experimentally for spin-3/2 nuclei and is a reasonable approximation for spin-5/2 aluminium. We also used hyperfine constants of Ga and As derived from our experiments. By contrast, no data is available for the aluminium hyperfine constant, and it is estimated as $A^{\mathrm{Al}} \sim 10$ μeV from Eq. 4 of the main text by taking the electron density at the nucleus $|\psi(0)|^2$ to be ∼0.55 of its value for atomic aluminium[21]. Such a scaling factor was chosen because of the small atomic mass Z of aluminium and based on the results for III-V semiconductors where $|\psi(0)|^2$ normalized by its atomic value ranges from ∼0.55 for the light ^{31}P in InP (Ref.[22]) to ∼0.85 for the heavy ^{121}Sb in InSb (Ref.[23]).

The results of calculations for ^{27}Al show that even if the nuclei of the barriers have the same (large) polarization as in the QD, the hyperfine shift of aluminium is still small ($< 1\%$) for the studied dots. Such smallness is essentially due to the structure of the dot and is a combined effect of small electron penetration into the barriers, reduced aluminium molar fraction $x^{\mathrm{Al}} < 1$, and small hyperfine constant A^{Al}. Thus we conclude from Supplementary Fig. 8 that experimental and model results for aluminium are in qualitative agreement, but the accuracy of the measurements is not sufficient to use aluminium hyperfine shifts to monitor the spatial distribution of nuclear polarization between the QD and the barrier.

As expected, the results of the model calculations for Ga and As show that isotope contributions to E_{hf} are constant if the barriers are not polarized and exhibit dependence on electron wavefunction confinement (parameterized by the ground state photoluminescence energy) when the barriers are polarized. However, the predicted variation of the hyperfine shifts is less than 1%, comparable to the spread in experimental data.

To summarize, Supplementary Fig. 8 demonstrates excellent agreement between measured and calculated relative contributions of different isotopes to the hyperfine shifts. Such studies conducted with *non-selective* depolarization of the isotopes provide a good verification of the values of the electron hyperfine constants A and spin temperatures derived from the *selective* depolarization of individual nuclear spin transitions of each isotope (as in Supplementary Fig. 7). The *selective* depolarization measurements appear to be more sensitive to the spatial distribution of the nuclear polarization and reveal some difference in polarization degree P_{N} between the QD and the barrier nuclei. However, the present level of sensitivity is not sufficient to make quantitative conclusions about the nanoscale spatial distribution of the nuclear polarization between the dots and barrier and requires further effort.

---

[*] e.chekhovich@sheffield.ac.uk

[1] Atkinson, P., Zallo, E., and Schmidt, O. G. Independent wavelength and density control of uniform GaAs/AlGaAs quantum dots grown by infilling self-assembled nanoholes. *J. Appl. Phys.* **112**(5), 054303 (2012).

[2] Paravastu, A. K. and Reimer, J. A. Nuclear spin temperature and magnetization transport in laser-enhanced NMR of bulk GaAs. *Phys. Rev. B* **71**, 045215, Jan (2005).

[3] Eickhoff, M. and Suter, D. Pulsed optically detected NMR of single GaAs/AlGaAs quantum wells. *Journal of Magnetic Resonance* **166**(1), 69 – 75 (2004).

[4] Chekhovich, E. A., Kavokin, K. V., Puebla, J., Krysa, A. B., Hopkinson, M., Andreev, A. D., Sanchez, A. M., Beanland, R., Skolnick, M. S., and Tartakovskii, A. I. Structural analysis of strained quantum dots using nuclear magnetic resonance. *Nature Nanotech.* **7**, 646–650 (2012).

[5] Checkhovich, E. A., Glazov, M. M., Krysa, A. B., Hopkinson, M., Senellart, P., Lemaître, A., Skolnick, M. S., and Tartakovskii, A. I. Element-sensitive measurement of the hole-nuclear spin interaction in quantum dots. *Nature Phys* **9**, 74–78 (2013).

[6] Munsch, M., Wust, G., Kuhlmann, A. V., Xue, F., Ludwig, A., Reuter, D., Wieck, A. D., Poggio, M., and Warburton, R. J. Manipulation of the nuclear spin ensemble in a quantum dot with chirped magnetic resonance pulses. *Nature Nanotechnology* **9**, 671–675 (2014).

[7] Chekhovich, E. A., Hopkinson, M., Skolnick, M. S., and Tartakovskii, A. I. Suppression of nuclear spin bath fluctuations in self-assembled quantum dots induced by inhomogeneous strain. *Nat Commun* **6**, 6348 (2015).

[8] Waeber, A. M., Hopkinson, M., Farrer, I., Ritchie, D. A., Nilsson, J., Stevenson, R. M., Bennett, A. J., Shields, A. J., Burkard, G., Tartakovskii, A. I., Skolnick, M. S., and Chekhovich, E. A. Few-second-long correlation times in a quantum dot nuclear spin bath probed by frequency-comb nuclear magnetic resonance spectroscopy. *Nature Phys* **12**, 688–693 (2016).

[9] Ulhaq, A., Duan, Q., Zallo, E., Ding, F., Schmidt, O. G., Tartakovskii, A. I., Skolnick, M. S., and Chekhovich, E. A. Vanishing electron g factor and long-lived nuclear spin polarization in weakly strained nanohole-filled GaAs/AlGaAs quantum dots. *Phys. Rev. B* **93**, 165306, Apr (2016).

[10] Bayer, M., Stern, O., Kuther, A., and Forchel, A. Spectroscopic study of dark excitons in $\mathrm{In}_x\mathrm{Ga}_{1-x}\mathrm{As}$ self-assembled quantum dots by a magnetic-field-induced symmetry breaking. *Phys. Rev. B* **61**, 7273–7276 (2000).

[11] Chekhovich, E. A., Krysa, A. B., Skolnick, M. S., and Tartakovskii, A. I. Direct measurement of the hole-nuclear spin interaction in single InP/GaInP quantum dots using photoluminescence spectroscopy. *Phys. Rev. Lett.* **106**, 027402 (2011).

[12] Puebla, J., Chekhovich, E. A., Hopkinson, M., Senellart, P., Lemaître, A., Skolnick, M. S., and Tartakovskii, A. I. Dynamic nuclear polarization in InGaAs/GaAs and GaAs/AlGaAs quantum dots under nonresonant ultralow-power optical excitation. *Phys. Rev. B* **88**, 045306 (2013).

[13] Latta, C., Högele, A., Zhao, Y., Vamivakas, A. N., Maletinsky, M., Kroner, M., Dreiser, J., Carusotto, I., Badolato, A., Schuh, D., Wegscheider, W., Atatture, M., and Imamoglu, A. Confluence of resonant laser excitation and bidirectional quantum-dot nuclear-spin plarization. *Nat Phys* **5**, 758 – 763 (2009).

[14] Chekhovich, E. A., Makhonin, M. N., Kavokin, K. V., Krysa, A. B., Skolnick, M. S., and Tartakovskii, A. I. Pumping of nuclear spins by optical excitation of spin-forbidden transitions in a quantum dot. *Phys. Rev. Lett.* **104**, 066804 (2010).

[15] Lai, C. W., Maletinsky, P., Badolato, A., and Imamoglu, A. Knight-field-enabled nuclear spin polarization in single quantum dots. *Phys. Rev. Lett.* **96**, 167403 (2006).

[16] Pfeiffer, M., Lindfors, K., Zhang, H., Fenk, B., Phillipp, F., Atkinson, P., Rastelli, A., Schmidt, O. G., Giessen, H., and Lippitz, M. Eleven nanometer alignment precision of a plasmonic nanoantenna with a self-assembled GaAs quantum dot. *Nano Letters* **14**(1), 197–201 (2014).

[17] Grundmann, M., Stier, O., and Bimberg, D. InAs/GaAs pyramidal quantum dots: Strain distribution, optical phonons, and electronic structure. *Phys. Rev. B* **52**, 11969–11981 (1995).

[18] Paget, D. Optical detection of nmr in high-purity GaAs: Direct study of the relaxation of nuclei close to shallow donors. *Phys. Rev. B* **25**, 4444–4451, Apr (1982).

[19] Eberhardt, K. W., Mouaziz, S., Boero, G., Brugger, J., and Meier, B. H. Direct observation of nuclear spin diffusion in real space. *Phys. Rev. Lett.* **99**, 227603, Nov (2007).

[20] Nikolaenko, A. E., Chekhovich, E. A., Makhonin, M. N., Drouzas, I. W., Van'kov, A. B., Skiba-Szymanska, J., Skolnick, M. S., Senellart, P., Martrou, D., Lemaître, A., and Tartakovskii, A. I. Suppression of nuclear spin diffusion at a $\mathrm{GaAs/Al}_x\mathrm{Ga}_{1-x}\mathrm{As}$ interface measured with a single quantum-dot nanoprobe. *Phys. Rev. B* **79**, 081303 (2009).

[21] Bennett, L. H., Watson, R. E., and Carter, G. C. Relevance of knight shift measurements to the electronic density of states. *Journal of research of the National Bureau of Standards - A. Physics and Chemistry* **74A**, 569–610 (1970).

[22] Gotschy, B., Denninger, G., Obloh, H., Wilkening, W., and Schnieder, J. Overhauser shift and dynamic nuclear polarization in InP. *Solid State Communications* **71**(7), 629–632 (1989).

[23] Gueron, M. Density of the conduction electrons at the nuclei in indium antimonide. *Phys. Rev.* **135**, A200–A205, Jul (1964).